nature photonics

LETTERS

https://doi.org/10.1038/s41566-018-0220-6

Spin control in reduced-dimensional chiral perovskites

Guankui Long[1,2,8], Chongyun Jiang[2,8], Randy Sabatini[1,8], Zhenyu Yang[1], Mingyang Wei[1], Li Na Quan[1], Qiuming Liang[3], Abdullah Rasmita[2], Mikhail Askerka[1], Grant Walters[1], Xiwen Gong[1], Jun Xing[2], Xinglin Wen[2], Rafael Quintero-Bermudez[1], Haifeng Yuan[1], Guichuan Xing[4], X. Renshaw Wang[2], Datong Song[3], Oleksandr Voznyy[1], Mingtao Zhang[5], Sjoerd Hoogland[1], Weibo Gao[2,6,7]*, Qihua Xiong[2,6]* and Edward H. Sargent[1]*

Hybrid organic–inorganic perovskites exhibit strong spin–orbit coupling[1], spin-dependent optical selection rules[2,3] and large Rashba splitting[4–8]. These characteristics make them promising candidates for spintronic devices[9] with photonic interfaces. Here we report that spin polarization in perovskites can be controlled through chemical design as well as by a magnetic field. We obtain both spin-polarized photon absorption and spin-polarized photoluminescence in reduced-dimensional chiral perovskites through combined strategies of chirality transfer and energy funnelling. A 3% spin-polarized photoluminescence is observed even in the absence of an applied external magnetic field owing to the different emission rates of σ^+ and σ^- polarized photoluminescence. Three-dimensional perovskites achieve a comparable degree of photoluminescence polarization only under an external magnetic field of 5 T. Our findings pave the way for chiral perovskites as powerful spintronic materials.

Spintronics[9] is an enabler of quantum information technology, especially quantum computing[10,11]. Whereas conventional electronics relies on the generation and transfer of charge, spintronics makes use of the electron's spin. For spintronic devices it is necessary to control the number of electrons in the well-defined spin state, that is, to establish spin polarization control. Candidate materials with large spin–orbit interactions are of particular interest. Their electrons can be excited with spin-polarized (SP) light, which transfers angular momentum and thus builds up spin accumulation, leading to electron occupation on spin-polarized states in the materials. Furthermore, the excited spin-polarized states can be converted into spin-polarized photoluminescence (SPPL). These phenomena have been observed in gallium arsenide (GaAs), a benchmark material for spintronics[12–14]. The development of low-temperature-fabricated, solution-processed spintronic materials will facilitate the deployment of these materials on a wide range of substrates, and avoid the need for epitaxial growth.

Hybrid organic–inorganic perovskites (HOIPs) have demonstrated a number of attractive properties, including long-range balanced charge carrier diffusion lengths[15], high dielectric constants[16], low trap densities[17] and tunable absorption and emission wavelengths[18]. These superior optical and electrical properties have prompted intensive research interest into these HOIPs for high-performance optoelectronics, including in photovoltaics[19–21], light-emitting diodes[22,23], lasers[18,24] and photodetectors[25,26].

The investigation of HOIPs in spintronics was launched only recently[2,3,27–29]. Perovskites have been found to exhibit strong spin–orbit coupling[1], spin-dependent optical selection rules[2,3] and large Rashba splitting[4–8], as well as significant magneto-photocurrent, magneto-electroluminescence and magneto-photoluminescence responses[1,30,31]. In particular, an unexpectedly long spin lifetime exceeding 1 ns and ultra-long spin-diffusion lengths of ~85 nm have recently been observed in HOIPs[27]. These properties suggest that HOIPs are promising materials for the next generation of spintronic devices.

The flexible crystal structure and ionic composition of HOIPs suggest strategies to define material properties at the time of design and synthesis. Specifically, HOIPs can potentially incorporate chiral organic ligands[32]. In 2006, Billing and colleagues reported the synthesis of chiral two-dimensional (2D) perovskite single crystals that incorporated chiral ligands[32], and in 2017, thin films of chiral 2D perovskites were prepared and shown to absorb spin-polarized light[33]. However, 2D perovskite films have so far exhibited poor photoluminescence quantum yields (PLQYs) due to significant nonradiative recombination[34], and this significantly impedes their potential in optoelectronic applications.

Fortunately, quasi-2D (also known as 'Ruddlesden–Popper' structural) perovskites have recently shown high PLQYs for efficient photo- and electrically induced light emission[22,23]. Excitonic funnelling assembled within quasi-2D perovskites is efficient for exciton transfer for radiative recombination, yet a question remains as to whether chirality transfer can be expected. We focus here on $\langle n \rangle = 2$ reduced-dimensional chiral perovskites (RDCPs, where $\langle n \rangle$ is the average number of inorganic layers separated by the bulky organic ligands) with the goal of maintaining a large fraction of the chiral organic component in the material and thus increasing the likelihood of chirality transfer.

In this study, we demonstrate that RDCPs exhibit both circular dichroism and SPPL without the use of an external magnetic field.

[1]Department of Electrical and Computer Engineering, University of Toronto, Toronto, Ontario, Canada. [2]Division of Physics and Applied Physics, School of Physical and Mathematical Sciences, Nanyang Technological University, Singapore, Singapore. [3]Department of Chemistry, University of Toronto, Toronto, Ontario, Canada. [4]Institute of Applied Physics and Materials Engineering, University of Macau, Macao , China. [5]College of Chemistry, Nankai University, Tianjin, China. [6]MajuLab, CNRS–Université de Nice–NUS–NTU International Joint Research Unit UMI 3654, Singapore, Singapore. [7]The Photonics Institute and Centre for Disruptive Photonic Technologies, Nanyang Technological University, Singapore, Singapore. [8]These authors contributed equally to this work: Guankui Long, Chongyun Jiang, Randy Sabatini. *e-mail: wbgao@ntu.edu.sg; qihua@ntu.edu.sg; ted.sargent@utoronto.ca

We began by synthesizing pure chiral 2D perovskites ($\langle n\rangle = 1$) and RDCPs ($\langle n\rangle = 2$) by incorporating chiral organic ligands. In this case, *R*- and *S*-methylbenzylammonium bromide (*R*-MBABr and *S*-MBABr, chemical structures shown in Fig. 1) are used as the chiral ligands, and racemic methylbenzylammonium bromide (*rac*-MBABr) is used to prepare achiral perovskites as controls. The introduction of these ligands forces the otherwise 3D perovskite into mixed reduced-dimensional layered structures[22,23]. A distribution of $\langle n\rangle$ values present in the RDCP samples is expected to produce efficient energy funnelling to the lowest-bandgap species[22,23].

Because $\langle n\rangle = 1$ perovskite contains the largest mole fraction of chiral ligands (as shown in Supplementary Fig. 1), it might be expected that chiral 2D perovskites ($\langle n\rangle = 1$) would exhibit the strongest chirality (as shown in Supplementary Fig. 2). However, no photoluminescence was observed for the pure chiral 2D $(MBA)_2PbBr_4$ ($\langle n\rangle = 1$) sample, in line with the very poor photoluminescence properties representative of many pure 2D perovskites[34]. We focus here on $\langle n\rangle = 2$ RDCPs with the goal of achieving both higher PLQY and strong chirality.

We first applied circular dichroism (CD) spectroscopy to confirm the chirality of *R*- and *S*-MBABr bromide salts, where the ellipticity (θ, in mdeg) is calculated based on equation (1):

$$\theta(\text{mdeg}) = \Delta A\left(\frac{\ln 10}{4}\right)\left(\frac{180,000}{\pi}\right) \quad (1)$$

where ΔA is the absorption difference of the left- and right-handed spin-polarized light[35,36]. As shown in Fig. 1b, opposite CD absorption features are observed in the two chiral ligands (the wider range linear absorption and CD spectra are shown in Supplementary Fig. 3). We conclude that the chiral ligands lead to the expected preferential absorption of the opposite handedness of spin-polarized light. The racemic blend of *R*- and *S*-MBABr ligands exhibits no absorption difference between left- and right-handed spin-polarized light. The CD signals for the chiral ligands do not extend past 280 nm; however, when they are incorporated into the RDCP, the resulting perovskites exhibit strongly spin-polarized absorption (induced CD) in the visible region (Fig. 1c). These observations indicate that the chirality of the organic ligands is successfully transferred to the perovskite quantum wells of which they are constituents. Here again, the *rac*-RDCP sample exhibits no CD signal. For *R*- and *S*-RDCPs, the CD signals exhibit dispersive features centred around the absorption energy (Supplementary Fig. 4). This is known as the 'Cotton effect' and is due to coupling between degenerate transition dipoles, and has been observed for many types of chiral material[35–38]. Conversely, no appreciable spin-polarized absorption peaks were observed for the higher dimensional species ($\langle n\rangle \geq 2$), revealing that the 2D component is the main contributor to the spin-polarized absorption.

We also examined the crystallinity and lattice orientations of perovskite domains using 2D grazing-incidence wide-angle X-ray scattering (2D-GIWAXS). As shown in Fig. 2a–c, the GIWAXS results confirm that all three samples (*rac*-RDCP, *R*-RDCP and *S*-RDCP) contain domains with both $\langle n\rangle = 1$ and larger $\langle n\rangle$ values. The samples exhibit similar scattering patterns, suggesting that they share similar crystal types and components. The $(002)_{n=1}$ scattering of the $\langle n\rangle = 1$ perovskite domain (that is, $(MBA)_2PbBr_4$) can be identified at scattering wavevector $q = 0.42$ Å^{-1}, corresponding to

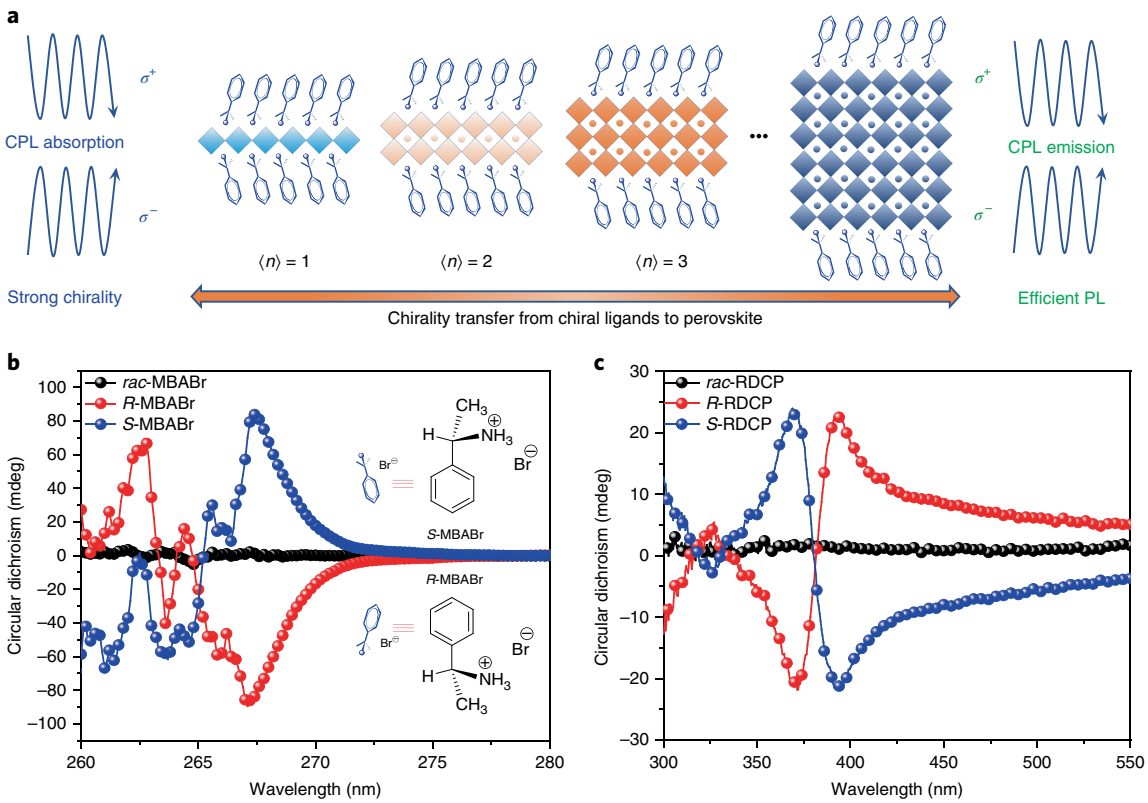

Fig. 1 | Chirality transfer and energy funnelling for efficient photoluminescence. a, Schematic illustration of the structures of RDCPs with different inorganic layers ($\langle n\rangle$). Chirality decreases with increasing $\langle n\rangle$ layers, and strong photoluminescence (PL) can be obtained through efficient energy funnelling to the higher $\langle n\rangle$ component. **b**, Circular dichroism (CD) spectra of the chiral ligands and a racemic mixture in dimethylformamide (0.5 mol l^{-1}). Inset, chemical structures of the chiral ligands (*R*-MBABr and *S*-MBABr) used in this work. **c**, Thin-film CD spectra of the RDCPs ($\langle n\rangle = 2$) prepared from the above chiral ligands.

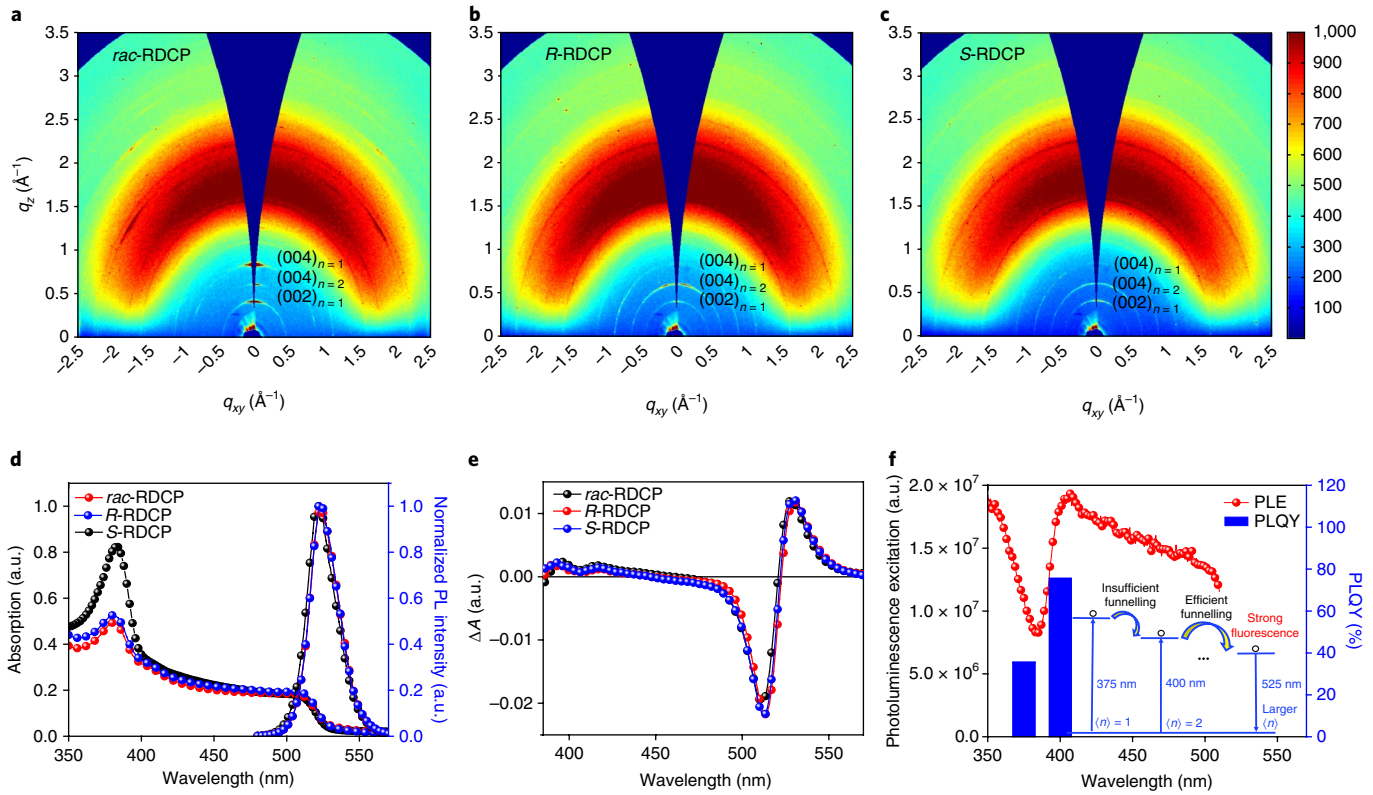

Fig. 2 | Structural and photophysical studies of RDCPs. a–c, 2D-GIWAXS results for ($\langle n\rangle = 2$) *rac*-RDCP (**a**), *R*-RDCP (**b**) and *S*-RDCP (**c**). **d**,**e**, Linear absorption and photoluminescence spectra (**d**) and transient absorption spectra (**e**) of *rac*-RDCP, *R*-RDCP and *S*-RDCP. **f**, Photoluminescence excitation spectra and PLQY of *rac*-RDCP under excitation wavelengths of 375 and 400 nm. Inset, diagram showing that energy funnelling from the $\langle n\rangle = 2$ component to the higher components is more efficient than that from the 2D perovskite component ($\langle n\rangle = 1$).

the $\langle n\rangle = 1$ interlayer distance of ~15 Å separating the chiral ligands (Supplementary Fig. 5)[32]. In addition, the peak at $q = 0.63$ Å^{-1} can be identified as the $(004)_{n=2}$ diffraction from the ($\langle n\rangle = 2$) quasi-2D perovskite layered domains with larger $\langle n\rangle$ (ref. [39]).

The presence of 2D and quasi-2D components in the RDCP films is further verified by the linear absorption spectra (Fig. 2d). The absorption feature at ~380 nm corresponds to the exciton peak of the 2D perovskite component (Supplementary Fig. 6), while the additional absorption extending to ~525 nm (absent in the pure 2D perovskite sample) corresponds to the higher $\langle n\rangle$ components ($\langle n\rangle \geq 2$).

These results confirm that all three samples (*rac*-RDCP, *R*-RDCP and *S*-RDCP) contain domains with both $\langle n\rangle = 1$ and larger $\langle n\rangle$ components. We sought next to study whether energy funnelling occurred among domains. We used ultrafast transient absorption spectroscopy (TAS) with a 350 nm pump pulse (10 μJ cm^{-2}, 1 kHz) to principally excite the $\langle n\rangle = 1$ component (Supplementary Fig. 7). From the spectra, following a 1 ps delay (Fig. 2e), we observe a strong bleach at ~511 nm, indicating that the energy has funnelled down to the component with the lowest bandgap. Interestingly, the photoluminescence excitation (PLE) spectrum (Fig. 2f) has a dip at ~380 nm, which belongs to the $\langle n\rangle = 1$ perovskite domains. This suggests that energy funnelling from higher $\langle n\rangle$ components is more efficient than from the 2D perovskite component (that is, $\langle n\rangle = 1$). This may be related to the characteristically poor photoluminescence of 2D perovskites that arises from their fast nonradiative rates[34]. The PLQY of the *rac*-RDCP was ~36% when photoexcited at 375 nm, whereas a higher PLQY of 76% was achieved when a 400 nm incident excitation pump was applied. The same trend was also seen in *R*-RDCP and *S*-RDCP, but the PLQY reaches an impressive 90% under 400 nm excitation.

The SPPL of chiral and achiral RDCPs was then measured using a fibre-based confocal microscope (Supplementary Fig. 8; for details of the optical set-up see Methods[40]). The measurements were performed at a temperature of 2 K with an applied magnetic field ranging from −7 T to 7 T perpendicular to the sample plane (Faraday configuration). As shown in Fig. 3a, the degree of polarization scales linearly with the magnetic field for the *rac*-RDCP sample; it exhibits zero DP at 0 T while the degree of polarization for both *R*- and *S*-RDCP is non-zero at 0 T (Fig. 3b,c). Compared with previous work on 3D perovskites[1], the *rac*-RDCPs exhibit a similar degree of polarization controlled via a magnetic field (Fig. 3a).

To explain the residual degree of polarization at $B = 0$ T observed for chiral perovskites, we refer to the energy level model shown in Fig. 4a,b. The model consists of the spin-up and spin-down electron minimum energy at the conduction band and its maximum energy at the valence band. Only the two spin-allowed transitions (for example, bright exciton transitions) are shown. In the case of achiral perovskite, these two transitions have the same spin-polarized emission rates, but this is not the case for chiral perovskites. Because the emission for RDCPs only originates from one excited state (the higher $\langle n\rangle$) to the ground state, the system is effectively a two-level system. For this case, based on Einstein coefficients[41], the different absorption rate of the spin-polarized light (Fig. 1c) for *R*-RDCP (or *S*-RDCP) implies a different spin-polarized emission rate (for example, $\gamma_{exc1} \neq \gamma_{exc2}$, as shown in Fig. 4). Thus, the *R*-RDCP (or *S*-RDCP) selectively emits σ^+ (or σ^-) polarized photoluminescence without the need for an external magnetic field.

The linear slope in Fig. 3 can be explained through the Zeeman effect. At non-zero magnetic field, the Zeeman effect breaks time-reversal symmetry in the system and gives rise to energy splitting of the spin subbands. As shown in Fig. 4c, when a positive magnetic field

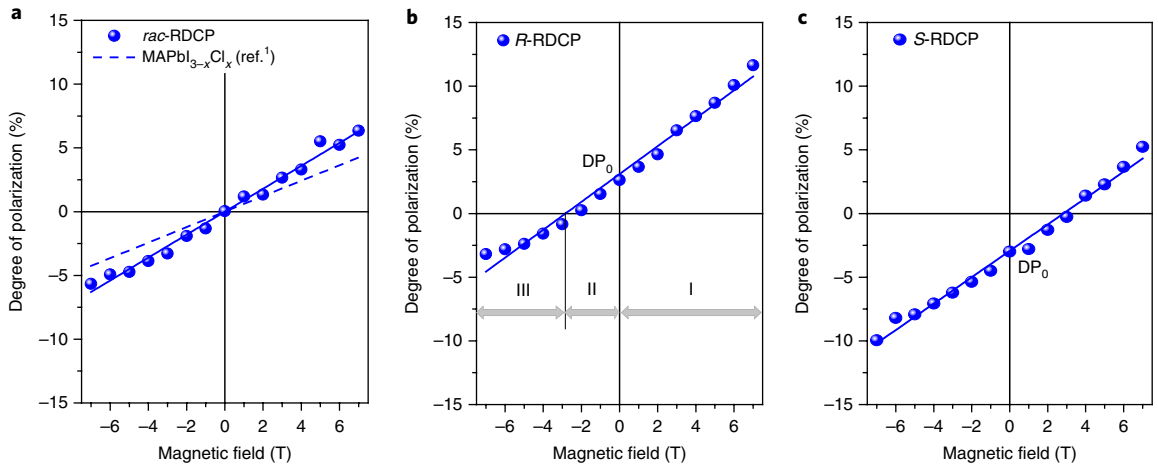

Fig. 3 | Polarized photoluminescence studies of RDCPs at 2 K. a–**c**, Degree of photoluminescence polarization for *rac*-RDCP (**a**), *R*-RDCP (**b**) and *S*-RDCP (**c**) with magnetic field varied from −7 T to 7 T. The blue line is fitting based on equation (2). The blue dashed line in **a** is the degree of polarization of 3D perovskite measured in ref. [1]. The graph of *R*-RDCP is devided into three regions: I, II and III. At $B = 0$ (no external magnetic field), there is a degree of polarization (DP_0) for *R*-RDCP. When a positive magnetic field is applied, the degree of polarization increases with the magnetic field (region I). In region II, as a negative magnetic field is applied, the degree of polarization decreases accordingly until it is zero. As a stronger negative magnetic field is applied, the degree of polarization changes sign from positive to negative (region III). Opposite phenomena are observed for *S*-RDCP.

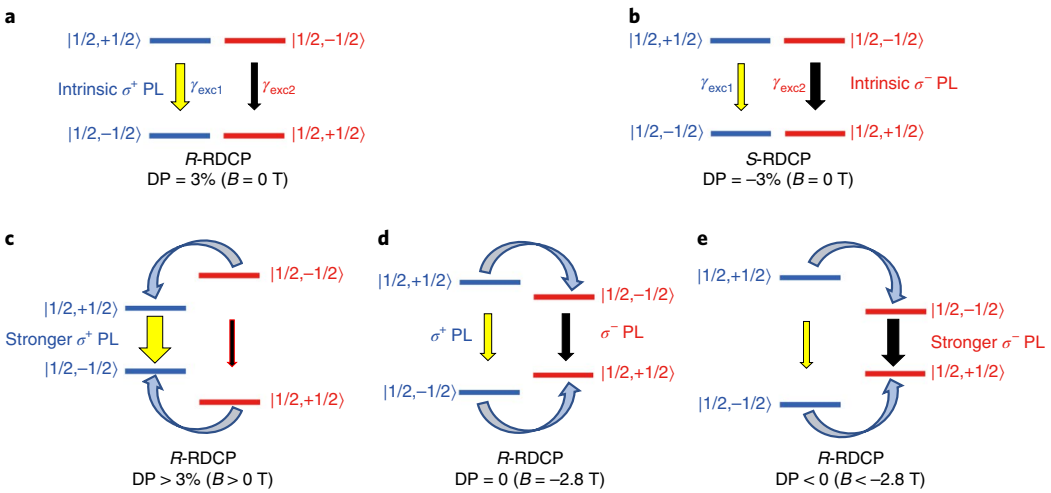

Fig. 4 | Mechanism of SPPL in RDCPs and the influence of magnetic field on the energy levels and degree of polarization of *R*-RDCP. a,**b**, Spin-up and spin-down energy levels for *R*-RDCP (**a**) and *S*-RDCP (**b**) without a magnetic field, and their relationship with the polarization of the photoluminescence. **c**, When a positive magnetic field is applied, the synergistic effect of Zeeman splitting and the asymmetric emission efficiency of *R*-RDCP further enhances the photoluminescence polarization, and thus more σ^+ polarized photoluminescence is obtained (region I in Fig. 3b). **d**,**e**, The degree of polarization (DP) decreases when applying a negative magnetic field (Fig. 3b, regions II and III, where $B < 0$ T) because the influence of the negative magnetic field and the chirality are opposite. **d**, When B is −2.8 T, the influence of the chirality transfer and Zeeman splitting cancels, and zero degree of polarization is observed (Fig. 3b). **e**, With further increase in the negative magnetic field, the influence of Zeeman splitting becomes dominant. Therefore, the photoluminescence polarization changes from σ^+ to σ^-, and negative degree of polarization is observed (Fig. 3b, region III, where $B < -2.8$ T). Yellow arrows indicate σ^+ polarized emission and black arrows indicate σ^- polarized emission, and the intensity is demonstrated by the width of the arrow. The emission rates of σ^+ (γ_{exc1}) and σ^- (γ_{exc2}) polarized photoluminescence for RDCPs are also shown in **a** and **b** for comparison.

is applied to *R*-RDCP, the spin degeneracy is lifted by the Zeeman splitting. At the valence band, the spin-up level becomes shallower than the spin-down level, while it is reversed at the conduction band. Therefore, spin flipping from spin-down to spin-up becomes thermodynamically favourable. The synergistic effect of Zeeman splitting under a positive magnetic field and the asymmetric emission efficiency further enhances the degree of photoluminescence polarization with increasing positive magnetic field (Fig. 3b, region I, $B > 0$ T). The value is reversed once a negative magnetic field is applied. As shown in Fig. 4d,e, energy splitting between spin-up and spin-down levels becomes larger with increasing negative magnetic field. The direction of spin flipping is reversed compared with that under a positive magnetic field, and the flipping from spin-up to spin-down energy level becomes energetically favourable. Because the influence of negative magnetic field and chirality transfer is opposite, the degree of polarization decreases with increasing negative magnetic field (Fig. 3b, regions II and III, where $B < 0$ T). When B is −2.8 T, the influence of chirality and Zeeman splitting cancels and zero degree

of polarization is observed (Figs. 3b and 4d). With a further increase in the strength of the negative magnetic field, the Zeeman splitting effect gradually dominates, and the photoluminescence polarization changes correspondingly from σ^+ to σ^- with the emergence of a negative degree of polarization (Fig. 3b, region III, where $B < -2.8$ T and Fig. 4e). As for *S*-RDCP, the total process is the opposite. However, for *rac*-RDCP, there is only Zeeman splitting (as observed in 3D perovskites) because of their centrosymmetric nature[1].

The magnetic field dependence results for these three samples (Fig. 3) are fitted following equation (2) (see Supplementary Note 3 for the detailed derivation):

$$\mathrm{DP} = \frac{g_{\mathrm{eff}}\mu_{\mathrm{B}}B}{k_{\mathrm{B}}T} + \mathrm{DP}_0 \quad (2)$$

where g_{eff} is the effective *g* factor of the spin-1/2 electron and hole in the spin-pair species (Supplementary equation (12)), μ_{B} is the Bohr magneton, B is the applied magnetic field, DP_0 is the degree of polarization introduced by the chirality in the absence of the magnetic field (Supplementary equation (13)), k_{B} is the Boltzmann constant and T is temperature. The g_{eff} values for the *R*-, *S*- and *rac*-RDCPs are 0.032, 0.031 and 0.027, respectively. The degree of polarization is ~3% for both *R*- and *S*-RDCP at 0 T, comparable to the previously reported experimental value of ~3% for 3D perovskites at 5 T (ref. [1]).

In summary, we report the control of spin-polarized absorption and photoluminescence in perovskites through material design. By combining chirality transfer and energy funnelling, we achieved 3% SPPL in RDCPs without the application of an external magnetic field. Compared with 3D perovskite, the same degree of photoluminescence polarization is obtained only under an external magnetic field of 5 T. RDCPs, which now combine the excellent optoelectronic properties and the function of chirality, would be of great interest in the field of spintronics.

Methods

Methods, including statements of data availability and any associated accession codes and references, are available at https://doi.org/10.1038/s41566-018-0220-6.

Received: 26 January 2018; Accepted: 3 July 2018;
Published online: 13 August 2018

References

1. Zhang, C. et al. Magnetic field effects in hybrid perovskite devices. *Nat. Phys.* **11**, 427–434 (2015).
2. Odenthal, P. et al. Spin-polarized exciton quantum beating in hybrid organic–inorganic perovskites. *Nat. Phys.* **13**, 894–899 (2017).
3. Giovanni, D. et al. Highly spin-polarized carrier dynamics and ultralarge photoinduced magnetization in $CH_3NH_3PbI_3$ perovskite thin films. *Nano Lett.* **15**, 1553–1558 (2015).
4. Niesner, D. et al. Giant Rashba splitting in $CH_3NH_3PbBr_3$ organic–inorganic perovskite. *Phys. Rev. Lett.* **117**, 126401 (2016).
5. Zhai, Y. et al. Giant Rashba splitting in 2D organic–inorganic halide perovskites measured by transient spectroscopies. *Sci. Adv.* **3**, e1700704 (2017).
6. Kim, M., Im, J., Freeman, A. J., Ihm, J. & Jin, H. Switchable $S=1/2$ and $J=1/2$ Rashba bands in ferroelectric halide perovskites. *Proc. Natl Acad. Sci. USA* **111**, 6900–6904 (2014).
7. Isarov, M. et al. Rashba effect in a single colloidal $CsPbBr_3$ perovskite nanocrystal detected by magneto-optical measurements. *Nano Lett.* **17**, 5020–5026 (2017).
8. Mosconi, E., Etienne, T. & De Angelis, F. Rashba band splitting in organohalide lead perovskites: bulk and surface effects. *J. Phys. Chem. Lett.* **8**, 2247–2252 (2017).
9. Pulizzi, F. Spintronics. *Nat. Mater.* **11**, 367 (2012).
10. Chappert, C., Fert, A. & Van Dau, F. N. The emergence of spin electronics in data storage. *Nat. Mater.* **6**, 813–823 (2007).
11. Ohno, Y. et al. Electrical spin injection in a ferromagnetic semiconductor heterostructure. *Nature* **402**, 790–792 (1999).
12. Ghali, M., Ohtani, K., Ohno, Y. & Ohno, H. Generation and control of polarization-entangled photons from GaAs island quantum dots by an electric field. *Nat. Commun.* **3**, 661 (2012).
13. Fiederling, R. et al. Injection and detection of a spin-polarized current in a light-emitting diode. *Nature* **402**, 787–790 (1999).
14. Edelstein, V. M. Spin polarization of conduction electrons induced by electric current in two-dimensional asymmetric electron systems. *Solid State Commun.* **73**, 233–235 (1990).
15. Stranks, S. D.et al. Electron–hole diffusion lengths exceeding 1 micrometer in an organometal trihalide perovskite absorber. *Science* **342,** 341–344 2013).
16. Juarez-Perez, E. J. et al. Photoinduced giant dielectric constant in lead halide perovskite solar cells. *J. Phys. Chem. Lett.* **5**, 2390–2394 (2014).
17. Shi, D. et al. Low trap-state density and long carrier diffusion in organolead trihalide perovskite single crystals. *Science* **347**, 519–522 (2015).
18. Zhu, H. et al. Lead halide perovskite nanowire lasers with low lasing thresholds and high quality factors. *Nat. Mater.* **14**, 636–642 (2015).
19. Eperon, G. E.et al. Perovskite–perovskite tandem photovoltaics with optimized band gaps. *Science* **354,** 861–865 2016).
20. Tsai, H. et al. High-efficiency two-dimensional Ruddlesden–Popper perovskite solar cells. *Nature* **536**, 312–316 (2016).
21. Bi, D. et al. Polymer-templated nucleation and crystal growth of perovskite films for solar cells with efficiency greater than 21%. *Nat. Energy* **1**, 16142 (2016).
22. Yuan, M. et al. Perovskite energy funnels for efficient light-emitting diodes. *Nat. Nanotech.* **11**, 872–877 (2016).
23. Wang, N. et al. Perovskite light-emitting diodes based on solution-processed self-organized multiple quantum wells. *Nat. Photon.* **10**, 699–704 (2016).
24. Zhang, Q., Ha, S. T., Liu, X., Sum, T. C. & Xiong, Q. Room-temperature near-infrared high-*Q* perovskite whispering-gallery planar nanolasers. *Nano Lett.* **14**, 5995–6001 (2014).
25. Lin, Q., Armin, A., Burn, P. L. & Meredith, P. Filterless narrowband visible photodetectors. *Nat. Photon.* **9**, 687–694 (2015).
26. Wei, H. et al. Sensitive X-ray detectors made of methylammonium lead tribromide perovskite single crystals. *Nat. Photon.* **10**, 333–339 (2016).
27. Sun, D. et al. Spintronics of organometal trihalide perovskites. Preprint at https://arxiv.org/abs/1608.00993 (2016).
28. Kepenekian, M. et al. Rashba and Dresselhaus effects in hybrid organic–inorganic perovskites: from basics to devices. *ACS Nano* **9**, 11557–11567 (2015).
29. Canneson, D. et al. Negatively charged and dark excitons in $CsPbBr_3$ perovskite nanocrystals revealed by high magnetic fields. *Nano Lett.* **17**, 6177–6183 (2017).
30. Hsiao, Y. C., Wu, T., Li, M. & Hu, B. Magneto-optical studies on spin-dependent charge recombination and dissociation in perovskite solar cells. *Adv. Mater.* **27**, 2899–2906 (2015).
31. Fu, M. et al. Neutral and charged exciton fine structure in single lead halide perovskite nanocrystals revealed by magneto-optical spectroscopy. *Nano Lett.* **17**, 2895–2901 (2017).
32. Billing, D. G. & Lemmerer, A. Synthesis and crystal structures of inorganic–organic hybrids incorporating an aromatic amine with a chiral functional group. *CrystEngComm* **8**, 686–695 (2006).
33. Ahn, J. et al. A new class of chiral semiconductors: chiral-organic-molecule-incorporating organic–inorganic hybrid perovskites. *Mater. Horiz.* **4**, 851–856 (2017).
34. Xing, G. et al. Transcending the slow bimolecular recombination in lead-halide perovskites for electroluminescence. *Nat. Commun.* **8**, 14558 (2017).
35. Riehl, J. P. & Richardson, F. S. Circularly polarized luminescence spectroscopy. *Chem. Rev.* **86**, 1–16 (1986).
36. Lightner, D. A. & Gurst, J. E. *Organic Conformational Analysis and Stereochemistry from Circular Dichroism Spectroscopy* Ch. 3 (Wiley, New York, NY, 2010).
37. Ben-Moshe, A., Teitelboim, A., Oron, D. & Markovich, G. Probing the interaction of quantum dots with chiral capping molecules using circular dichroism spectroscopy. *Nano Lett.* **16**, 7467–7473 (2016).
38. Schellman, J. A. & Oriel, P. Origin of the cotton effect of helical polypeptides. *J. Chem. Phys.* **37**, 2114–2124 (1962).
39. Slavney, A. H. et al. Chemical approaches to addressing the instability and toxicity of lead-halide perovskite absorbers. *Inorg. Chem.* **56**, 46–55 (2017).
40. Jiang, C. et al. Zeeman splitting via spin-valley-layer coupling in bilayer $MoTe_2$. *Nat. Commun.* **8**, 802 (2017).
41. Hilborn, R. C. Einstein coefficients, cross-sections, F values, dipole-moments, and all that. *Am. J. Phys.* **50**, 982–986 (1982).

Acknowledgements

This publication is based, in part, on work supported by an award (KUS-11-009-21) from the King Abdullah University of Science and Technology (KAUST), by the Ontario

Research Fund Research Excellence Program, by the Ontario Research Fund (ORF), and by the Natural Sciences and Engineering Research Council (NSERC) of Canada. W.G., C.J. and G.L. acknowledge support from the Singapore National Research Foundation through a 2015 NRF fellowship grant (NRF-NRFF2015-03), Singapore Ministry of Education via an AcRF Tier2 grant (nos. MOE2016-T2-2-077 and MOE2017-T2-1-163) and the A*Star QTE Programme. Q.X. acknowledges financial support from Singapore National Research Foundation via an Investigatorship Award (NRF-NRFI2015-03) and a Competitive Research Programme (NRF-CRP14-2014-03), and the Singapore Ministry of Education through AcRF Tier 2 and Tier 1 grants (MOE2015-T2-1-047 and RG 113/16). G.X. acknowledges financial support from Macau Science and Technology Development Fund (FDCT-116/2016/A3, FDCT-091/2017/A2), a Research Grant (SRG2016-00087-FST, MYRG2018-00148-IAPME) from the University of Macau, the Natural Science Foundation of China (91733302, 61605073 and 2015CB932200) and the Young 1000 Talents Global Recruitment Program of China. X.R.W. acknowledges support from a Nanyang Assistant Professorship grant from Nanyang Technological University and Academic Research Fund Tier 1 (RG108/17S) from the Singapore Ministry of Education. G.L. acknowledges the International Postdoctoral Exchange Fellowship Program of the Office of China Postdoctoral Council. H.Y. acknowledges the Research Foundation-Flanders (FWO Vlaanderen) for a postdoctoral fellowship. The authors thank A.S. Namin (QU), R.G. Sabat (QU), J.-M. Nunzi (QU), A. Xia (ICCAS) and X. Wang (ICCAS) for measuring the room-temperature SPPL. The authors thank C. Zhang (ICCAS) and Z.V. Vardeny (University of Utah) for helpful discussions. The authors also thank E. Palmiano, R. Wolowiec and D. Kopilovic for their help during the course of this study.

Author contributions

G.L., S.H. and E.H.S. conceived the idea and designed the experiments. G.L., R.S., Z.Y., W.G., Q.X. and E.H.S. wrote the manuscript. G.L. fabricated thin films with help from L.Q. and J.X. G.L. prepared chiral ammonium salts and performed measurements (CD, PL, PLE, PLQY, TAS and XRD) with help from R.S., G.W., M.W., X.G., Q.L. and D.S. R.S. and G.X. analysed the TAS data. Z.Y. and R.Q.-B. performed the GIWAXS measurement. C.J., W.G., X.L.W., Q.X., G.W. and H.Y. performed the SSPL measurement. C.J., A.R., W.G., M.W., G.L, M.Z., X.W., O.V. and M.A. performed the SSPL data analysis and discussion. A.R. built the mathematics model for magnetic field-dependent SPPL for RDCP. All authors read and commented on the manuscript.

Competing interests

The authors declare no competing interests.

Additional information

Supplementary information is available for this paper at https://doi.org/10.1038/s41566-018-0220-6.

Reprints and permissions information is available at www.nature.com/reprints.

Correspondence and requests for materials should be addressed to W.G. or Q.X. or E.H.S.

Publisher's note: Springer Nature remains neutral with regard to jurisdictional claims in published maps and institutional affiliations.

Methods

Thin-film fabrication. Predesigned amounts of $PbBr_2$ (183.5 mg, 0.5 mmol), CH_3NH_3Br (5.6 mg, 0.05 mmol), CsBr (42.5 mg, 0.2 mmol) and MBABr (101 mg, 0.5 mmol) were put into a small vial with 0.5 ml dimethyl sulfoxide. The solution was stirred at room temperature in a nitrogen-filled glovebox for 4 h, and then filtered through a polytetrafluoroethylene syringe filter (0.2 µm). The resulting solution was spin-coated onto the precleaned substrate via a two-step process at 1,000 r.p.m. (accelerate speed: 200 r.p.m.s^{-1}) and 5,000 r.p.m. (accelerate speed: 500 r.p.m.s^{-1}) for 10 s and 60 s, respectively. During the second spin step, 200 µl chlorobenzene was poured onto the substrate 20 s after spinning started. The resulting films were annealed at 90 °C for 10 min to improve crystallization. The thickness of the obtained perovskite film was ~600 nm.

Absorption, photoluminescence and PLE spectra and PLQY measurements. Optical absorption measurements were carried out in a Lambda 950 UV–vis spectrophotometer. A Horiba Fluorolog system was used for photoluminescence measurements. A monochromatized Xe lamp was used as the excitation source for steady-state photoluminescence collection. The Fluorolog system was coupled to a Quanta-Phi integrating sphere with optical fibre bundles for absolute PLQY measurements. Excitation and emission spectra were measured for three cases: the sample directly illuminated by the beam path in the integrating sphere, the sample indirectly illuminated within the integrating sphere, and the empty sphere. The Fluorolog was set to an excitation wavelength of 400 nm and 2 nm bandpass for both excitation and emission slits. The detector and integrating sphere were calibrated with a Newport white light source for spectral variance. PLE spectra were measured by monitoring the emission intensity as the excitation wavelength was varied. PLE spectra were normalized to the lamp intensity spectrum.

CD spectra. CD spectra were recorded on a JASCO J-810 CD spectrometer with 'Standard' sensitivity (100 mdeg) at 50 nm min^{-1} scan speed with 0.5 nm resolution and response time of 1 s. All measurements were performed at 20 °C.

Transient absorption measurements. Femtosecond laser pulses were created with a regeneratively amplified Yb:KGW laser at a 1 kHz repetition rate (Light Conversion, Pharos). A portion of the 1,030 nm fundamental was passed through an optical parametric amplifier (Light Conversion, Orpheus) with the second harmonic of the signal pulse selected for 350 nm light. Both the pump and residual fundamental were sent into an optical bench (Ultrafast, Helios), where the fundamental was focused into a calcium fluoride crystal, generating a white light continuum. The time delay (resolution ~350 fs) was set by delaying the probe pulse optically, with time steps increasing exponentially. A chopper was used to block every other pump pulse, and then the probe pulse was measured by a charge-coupled device (CCD) after being dispersed by a grating spectrograph (Ultrafast, Helios). Samples were spin-coated on a glass substrate, and were translated at 1 mm s^{-1} during the measurement. The pump fluences were held at 10 µJ cm^{-2}.

SPPL measurement under magnetic field. A homemade fibre-based confocal microscope was used for polarization-resolved magneto-photoluminescence spectroscopy. The wavelength of the excitation was 473 nm. Polarizers and quarter-wave plates were installed on the excitation and detection arms of the confocal microscope for polarization-resolved photoluminescence detection. Photoluminescence emission was directed by a multimode optical fibre into a spectrometer (Andor Technology). Samples were loaded into a magneto-cryostat (Cryomagnetics close-cycle cryostat) cooled to 2 K. A magnetic field was applied perpendicular to the sample plane (Faraday configuration) and ranged from −7 T to + 7 T, and the SPPL was collected along the direction of the magnetic field (Supplementary Fig. 8). σ^+ and σ^- polarized excitations were employed (Supplementary Fig. 9), and the averaged degree of polarization under σ^+ and σ^- polarized excitation is shown in Fig. 3.

To extract the polarization of the photoluminescence emission, we rotated the quarter-wave plate on the detection arm by 360° in steps of 10°. The photoluminescence (PL) intensity as a function of rotation angle can be written as

$$I_{PL} = S_3 \sin 2\varphi + S_0 \tag{3}$$

where S_3 and S_0 are the Stokes parameters corresponding to the circular polarization and the total intensity, respectively, and φ is the angle of the quarter-wave plate. The degree of polarization is therefore given by

$$DP = \frac{S_3}{S_0} = \frac{I_{\sigma^+} - I_{\sigma^-}}{I_{\sigma^+} + I_{\sigma^-}} \tag{4}$$

where I_{σ^+} and I_{σ^-} are the areas of the left- and right-handed spin-polarized emission under photoexcitation, respectively.

GIWAXS measurement. All GIWAXS measurements were conducted at the Hard X-ray MicroAnalysis (HXMA) beamline of the Canadian Light Source (CLS). An energy of 17.998 keV ($\lambda = 0.6888$ Å) was selected using a Si (111) monochromator. The incident angle was kept at 0.5° with respect to the sample plane. Patterns were collected on a SX165 CCD camera (Rayonix) placed at a distance of 175 mm from the sample. A lead beam stop was used to block the direct beam. Images were calibrated using LaB6 and processed with the Nika software package and GIXSGUI MATLAB plugin.

Data availability. The data that support the plots within this paper and other findings of this study are available from the corresponding authors upon reasonable request.